

One-pot synthesis of organic conductive nanoparticles with high photothermal conversion efficiency

Lorena Ruiz-Perez^{1,2}, Loris Rizzello¹, JinPing Wang⁴, Nan Li⁴,
Giuseppe Battaglia^{1,2,3,*}, Yiwen Pei^{5*}

¹Department of Chemistry, University College London, London, WC1H 0AJ, UK

²The EPSRC/JEOL Centre for Liquid Electron Microscopy, London, WC1H 0AJ, UK

³Department of Chemical Engineering, University College London, London, UK

⁴Tianjin Key Laboratory of Drug Delivery & High-Efficiency, School of Pharmaceutical Science and Technology, Tianjin University, 300072, PR China.

⁵Chemical Medical and Environmental Science Department, National Physical Laboratory, London, TW11 0LW, UK

*Email: g.battaglia@ucl.ac.uk; yiwen.pei@npl.co.uk

Organic conductive nanoparticles can directly harvest heat from light, making them desirable for photothermal ablation of cancerous cells.¹ Here we demonstrate the use of polymerization induced self-assembly (PISA) and conventional oxidative polymerization to produce a range of conducting polymer (CP) colloidal nanoparticles that allows to precisely control their nanostructures, leading to tailorable photothermal effects depending on the selected PISA templates and the reaction conditions used. Polypyrrole (PPy) and polyaniline (PANI) nanoparticles were readily synthesized in water by the chemical oxidation of the respective monomers using the Fe (III) complexed, PISA-prepared nano-objects as structure-directing templates. These particles exhibit strong absorption in the near infrared (NIR) region with excellent photothermal efficiencies, measured by UV-vis spectrometer and photothermal efficacy studies. The ability of these nanocomposites to act as bio-imaging tools is shown by fluorescent imaging studies, and their potential for applications as therapeutic agents is proven by cellular uptake and cell cytotoxicity studies.

Since the first report of electrically conducting polymers, ‘doped’ polyacetylene in 1977,² the research of conjugated polymers or synthetic metals has developed vastly. These highly versatile metal-like polymeric materials are currently receiving significant attention in fields such as energy storage,³ light-emitting diodes⁴ and biomedical devices.⁵ Owing to their excellent biocompatibility, large surface area and unique optical properties, PPy⁶ and PANI⁷ nanoparticles have been particularly exploited for the treatment of cancer in recent years, establishing an early precedent for *in vivo* use of CP nanoparticles.¹ When exposed to light, these nanomaterials can absorb photon energy and effectively convert it into heat, making them a promising candidate for photothermal therapy (PTT). Harnessing such an optical property for hyperthermia therapy, however, requires careful design of the nano-scale architecture, functionality and chemistry of CP particles to optimize their selectivity, photostability and photothermal conversion efficiency.

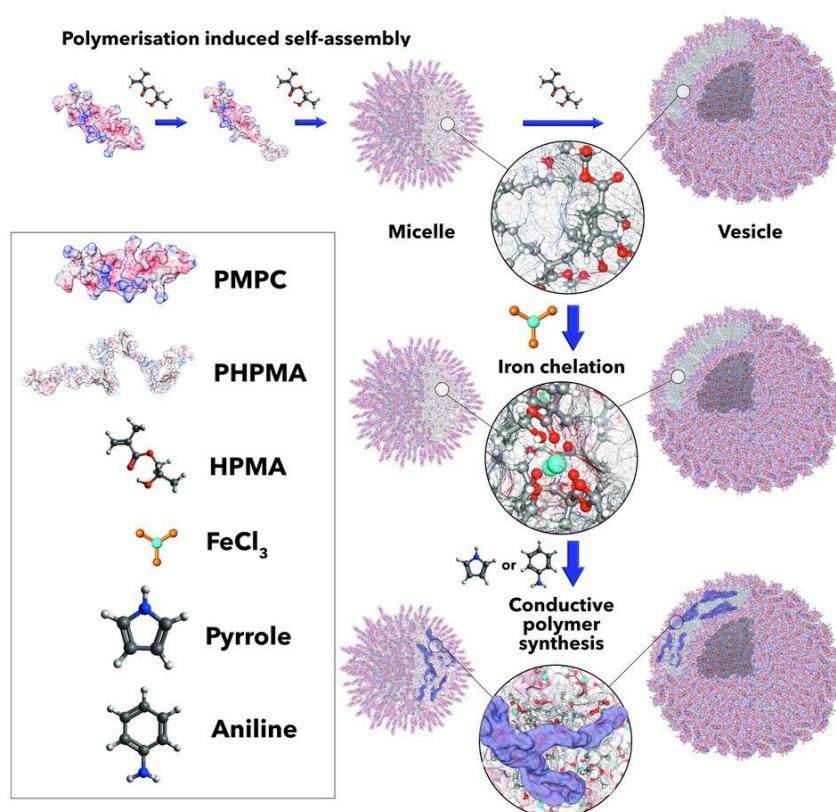
The increasing demand for CP-based colloidal nanoparticles has expedited the development of a range of synthetic strategies, including hard⁸ and soft templating⁹ and bottom-up approaches.¹⁰ However, each of these strategies comes with its own limitations. For example, the hard template method involves rather tedious steps and the subsequent removal of the templates often results in the deformation of the targeted products. The relatively cheap and powerful soft template method (*e.g.* emulsion technique) lacks control over the dimension and shape of targeted products. The template-free approach (*e.g.* dispersion polymerization) offers a desirable route to easy access to targeted nanostructures but it is hindered by limited accessibility to higher-ordered hierarchical nanostructures, such as tubes and vesicles.¹¹

More recently there has been a growing interest in a unique synthetic approach termed polymerisation-induced self-assembly (PISA) that allows for *simultaneous* block copolymer synthesis and *in situ* self-assembly.¹² In particular, it has been exploited to produce nanoparticles with higher-ordered hierarchical nanostructure at very high solids content (up to 50 wt%).¹³ Such a facile and scalable process has been exploited to prepare a range of hybrid polymer-inorganic nanoparticles, including silica,¹⁴ gold,¹⁵ and iron nanocomposites,¹⁶ by selective localization of metal or metal oxide precursor and then the post-PISA treatment. However, to the best of our knowledge, PISA technique has been rarely utilized to prepare polymer-organic hybrid nanoparticles.¹⁷

Herein we report the one-pot synthesis of polymeric semiconducting colloidal nanoparticles *via* the PISA process and chemical oxidative polymerization technique. Such a highly versatile approach allows us generating hybrid polymer-organic nanocomposites with variable nanostructures and tunable photothermal effects in a simple and scalable fashion, without the need to remove the templates. We also evaluate the capability of these semiconducting nanomaterials as a bio-imaging tool by means of *in vitro* fluorescence imaging studies and their biocompatibility *via* cellular uptake and cytotoxicity measurements. These experiments provide new insights towards the design criteria of functionalized CP-based nanoparticles for molecular imaging and targeted cancer therapy.

We selected the reversible addition-fragmentation chain-transfer (RAFT)-PISA prepared polymeric nanoparticles, which are based on amphiphilic AB diblock copolymers, poly[2-(methacryloyloxy)ethyl phosphorylcholine]-*block*-poly(2-hydroxypropyl methacrylate) (PMPC-*b*-PHPMA), as structure-directing templates.

Such a combination was chosen due to its ability to produce monodisperse nanoparticles in water with the highly biocompatible PMPC stabilizing chains on the surface. We also discovered that PMPC chains interact selectively with the scavenger receptor B1 making them selective towards antigen presenting cells (ref Colley et al Mol Pharm and Rizzello et al BiorXiv). Specifically, PHPMA block was selected as the absorbing block for CP owing to their unique ability to chelate the Fe^{3+} atoms. Thanks to its capability of partial hydration in water,¹⁸ the PHMA block also allows the entrapment of Fe^{3+} ions within the nanoparticles core. FeCl_3 is considered to be one of the appropriate oxidising agents to polymerise pyrrole¹⁹ and aniline²⁰. This is due to the fact that it has desirable solubility, *i.e.* soluble in both water and polar organic solvent, and the advantage of producing CP with excellent properties.²⁰ As shown in Scheme 1, simple mixing of FeCl_3 and PMPC-*b*-PHPMA aqueous dispersion allows the metal cations to bind to the lone electron pairs on the PHMPA chains forming a chelate complex. The iron cations/PHPMA chelate complex, in turn, facilitates the chemical oxidative polymerization of PPy and PANI within the PHPMA nanoparticles core, with the PMPC chains acting as the stabilising block.



Scheme 1. A schematic illustration of the one-pot synthesis of polypyrrole (PPy) and polyaniline (PANI) micelles and vesicles using polymerisation-induced self-assembly (PISA)-prepared PMPC-*b*-PHPMA diblock copolymers nano-objects as structure-directing templates.

TEM analysis has been used to investigate particle formation and also provide insights on the particle growth mechanisms. Using monodisperse PISA-prepared PMPC_{43} -*b*- PHPMA_{258} templates (Figure 1A), uniform PPy and PANI nanospheres can be successfully produced with diameters of 98 ± 10 nm and 100 ± 12 nm, respectively (Figure 1B&1C). The TEM measurements are in strong agreement with dynamic light scattering (DLS) hydrodynamic diameters of 192.3 nm ($\mu_2/I^2 = 0.21$) and 162.8 nm

($\mu_2/I^2 = 0.24$). The use of PMPC₁₅-*b*-PHPMA₄₄₅ PISA templates (Figure 1D) allows the successful formation of PPy and PANI nanovesicles (Figure 1E&1F) whose TEM-measured diameters of (118 ± 11) nm and (101 ± 8) nm are in reasonable agreement with those estimated by DLS of 190 nm ($\mu_2/I^2 = 0.23$) and 360 nm ($\mu_2/I^2 = 0.19$). The discrepancy between TEM and DLS results is not uncommon. It is indeed a direct illustration of the sizes being measured in the solid state (TEM) *versus* in solution (DLS).

To elucidate the respective roles played by the PMPC and PHPMA block during the growth of the CP particles, vesicular Fe³⁺-complexed PMPC-*b*-PHPMA particles were prepared *without* any pyrrole or aniline monomer. Energy Filtered TEM was utilised to chemically map the iron and phosphorus contents of these particles in absence of a staining agent (Figure 1G, 1J, 1K 1L&1M). Figure 1G&1L show the presence of Fe in the nanovesicles suggesting the complexation between Fe³⁺ and PHPMA blocks that ultimately directs the growth of CP. The location of Fe was nicely illustrated using scanning transmission electron microscopy (STEM) mode. Thanks to its atomic number, high contrast Fe can be easily visualized in the bilayer region of the nanovesicles (Figure 1H). Moreover, the appearance of phosphorous (Figure 1M) provides direct evidence that the PMPC stabilizing block remains intact and is intimately associated with the nanoparticles to provide colloidal stability and biocompatibility. In addition, height profiles obtained from thickness map, (Figure 1I) confirms the vesicular nanostructure after the post-PISA treatment.

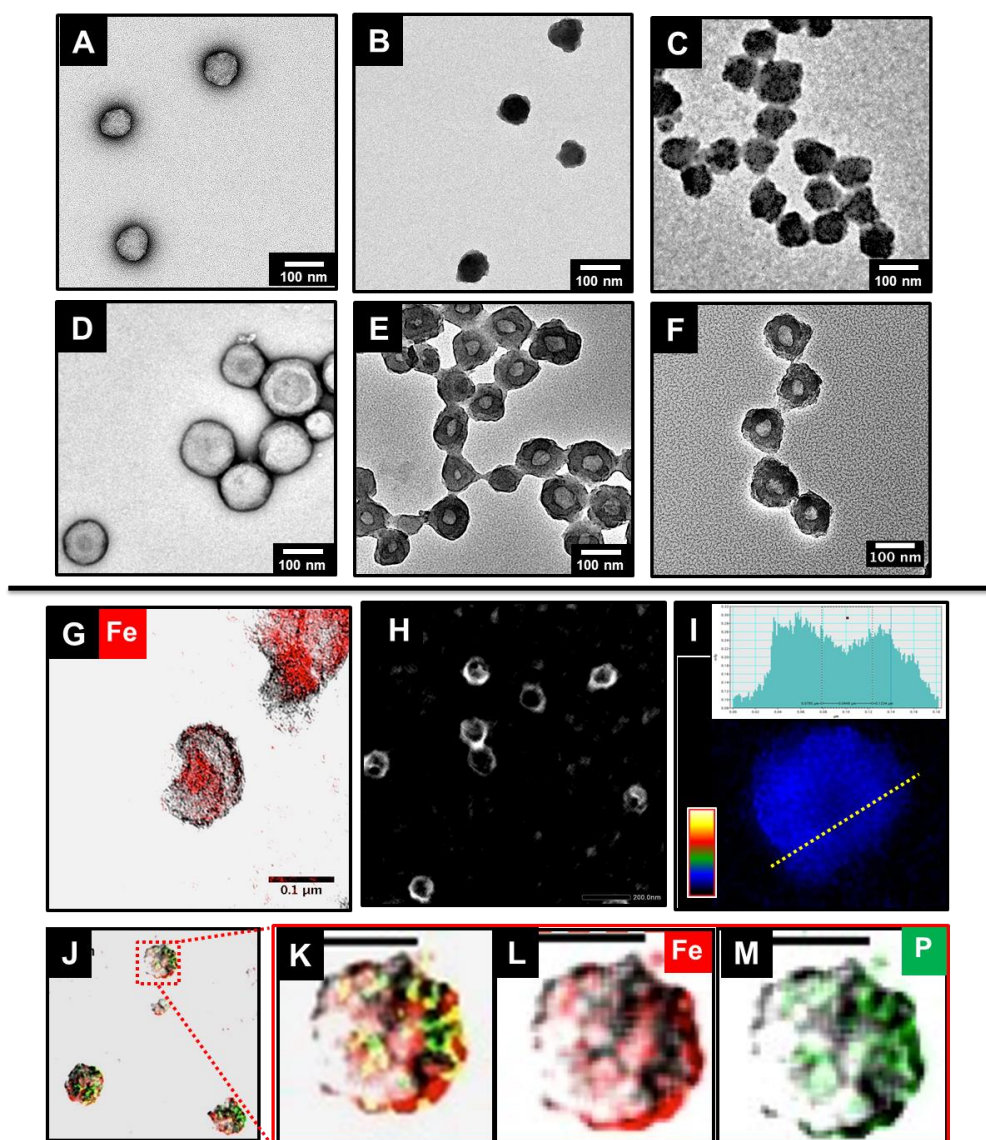


Figure 1. Conventional TEM micrographs of (A) PTA stained PMPC₄₃-*b*-HPMA₂₅₈ template structures showing sphere formation, (B) PPy- and (C) PANI-based PMPC₄₃-*b*-PHPMA₂₅₈ nanospheres; (D) PTA-stained PMPC₁₅-*b*-HPMA₄₄₅ template structures showing formation of nanovesicles, (E) PPy- and (F) PANI-based PMPC₁₅-*b*-HPMA₄₄₅ nanovesicles. For the Fe³⁺-complexed PMPC-*b*-PHPMA nanovesicles *without* any pyrrole or aniline monomer, energy filtered TEM micrographs displaying (G, L) Fe elemental map (red signal), (M) P elemental map (green signal) and (J, K) a combination of two elements superimposed to zero-loss image while (H) the STEM imaging in dark field highlights the iron content in the core due to its high contrast. (I) False colored thickness map of the Fe³⁺ complex CP-free nanovesicles displaying electron mean free path (mfp) color scale on the bottom right. Blue corresponds to mfp value of circa 1 indicating appropriate thickness for optimal elemental mapping. Inset top image: thickness profile across vesicle shows a thinner region in the core mirroring vesicular structures.

¹³C solid-state NMR, FTIR and UV-vis spectroscopy were performed to further confirm the formation of CP-based nanoparticles. In the FTIR spectra of PPy particles (Figure 2A), the bands found at 1550 cm⁻¹, 1350 cm⁻¹, 1005 cm⁻¹ and 950 cm⁻¹ are likely

attributed to stretching vibration of C=C units, C-N absorption, and =C-N in-plane and out-plane deformation vibration, respectively.²¹ For PANI particles, the characteristic peaks at 3390 cm⁻¹, 3020 cm⁻¹, 1590 cm⁻¹, 1290 cm⁻¹ 830 cm⁻¹ correspond to the N-H stretching vibration, aromatic C-H stretching, benzene/quinone ring deformation, C=N stretching of a secondary aromatic amine, and aromatic C-H out-of-plane bending.²² In Figure 2B, high-resolution solid-state ¹³C NMR shows the characteristic carbon resonance of *c.a.* 125 ppm which is associated with α - α' linkages of PPy²³ while two peaks at *c.a.* 120 ppm and *c.a.* 158 ppm were likely linked to C-C linkages and C=N quinoid resonance of PANI.²⁰ Strong absorption in the NIR window (650 nm-900 nm) is critical in designing therapeutical agents since the long-wavelength laser allows for noninvasive penetration of reasonably deep tissues.²⁴ Figure 2C shows the UV-vis spectra of copolymer templates, PPy and PANI particles in water (pH 7). The broad absorption bands extending from 600 nm to 900 nm were found for both PPy and PANI particles which is characteristic of the bipolaronic metallic state of doped CP.²⁵ With decrease of pH value in PANI nanovesicle dispersion, however, the main peak shifted from *c.a.* 580 nm to *c.a.* 750 nm indicating the transformation of PANI from its leucoemeraldine to the more conductive emeraldine form (Figure 2D).²⁶ This is accompanied by a drastic color change from purple to green upon changes in solution pH (inset image in Figure 2D).

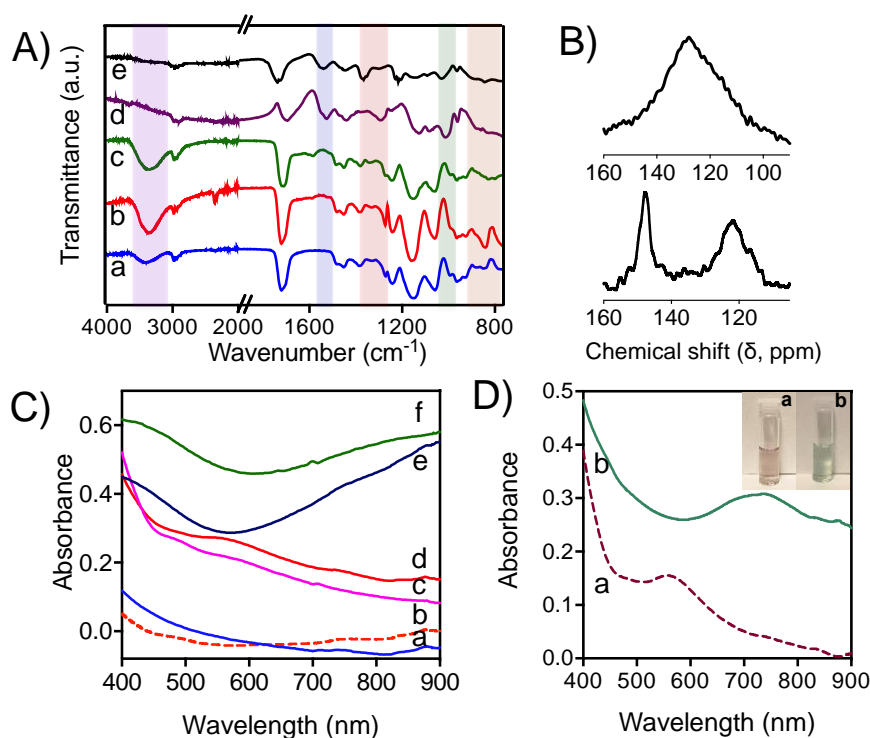


Figure 2. FT-IR spectra (A) of pure water (a), unmodified PMPC₄₃-*b*-PHPMA₂₅₈ particles suspension (b), PANI- and PPy-based nanospheres (c, e) and nanovesicles (d, h) suspension; ¹³C NMR spectra (B) of PPy (top) and PANI (bottom) nanospheres; UV/Vis spectra (C) of unmodified (a) and FeCl₃-treated (b) PMPC₄₃-*b*-PHPMA₂₅₈ particles, PANI- and PPy-based nanospheres (c, e) as well as nanovesicles (d, f); UV/Vis spectra (D) of pH-sensitive vesicular PANI particles in neutral (a) and acidic water (b). Inset images illustrate a drastic colour change of PANI particles in response to solution pH.

The photothermal effect induced by NIR light illumination was investigated by monitoring the temperature of CP dispersions irradiated by a NIR laser (808 nm, 1.5 W cm⁻²). Exposure to the NIR laser for 5 minutes led to a drastic increase of the solution temperature of all CP samples while the temperature of water has barely changed (Figure 3A). It is worth-noting that, at 0.2 mg mL⁻¹, these semiconducting colloids could reach 42 °C, sufficient to kill tumor cells.²⁷ We also observed that the PPy-based dispersions could reach higher temperatures (68.5 °C for nanospheres and 78.5 °C for nanovesicles) compared to the PANI-based ones (45.5 °C for nanospheres and 65.5 °C for nanovesicles). Moreover, the vesicular particles appeared to transduce more heat than the micellar ones under the same conditions. The photothermal images (Figure 3B) support and confirm these observations. The robustness and reproducibility of the observed photothermal effects were demonstrated by performing multiple cycles of NIR laser ON/OFF switch (Figure 3C). It is found that the temperature of CP-based colloids can be regulated within a relatively short time scale and these particles appeared to be photostable during the cycles (Figure SI). The differences in the photothermal performance between the PPy- and the PANI-based nanoparticles may be attributed to their difference in intrinsic conductivities²⁸ and relatively low NIR absorption of PANI in neutral water (Fig 2D).²⁶ It is well documented that morphology plays an important role on how efficient nanomaterial transduce light to heat.²⁹⁻³⁰ The enhanced photothermal effect observed in nanovesicles is likely due to their unique structure where the CP cores may capture more energy upon irradiation. Considering their hybrid nature, these composite nanomaterials exhibit relatively high photothermal efficiencies.³¹⁻³² These attractive features clearly make these nanomaterials a promising candidate for thermal ablation of cancer cells.

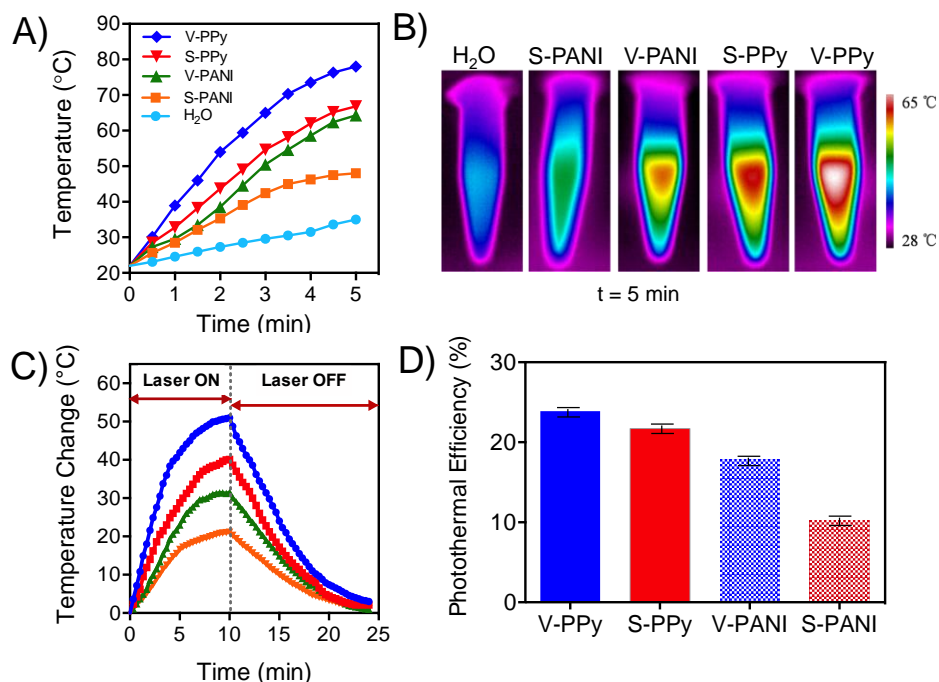


Figure 3. Photothermal transduction of PPy- and PANI-based nanospheres (S_PPy and S_PANI) and nanovesicles (V_PPy and V_PANI) dispersion. (A) Photothermal effect of the particles (1.0 mg mL⁻¹) upon irradiation with a laser of a wavelength at 808 nm and power of 2 W cm²; (B) Photothermal images after 5 min laser irradiation; (C) Temperature change in solution (0.2 mg mL⁻¹) after 10 min laser irradiation; (D) Mean

photothermal efficiency from the conversion of light to heat in CP-based nanoparticle solutions.

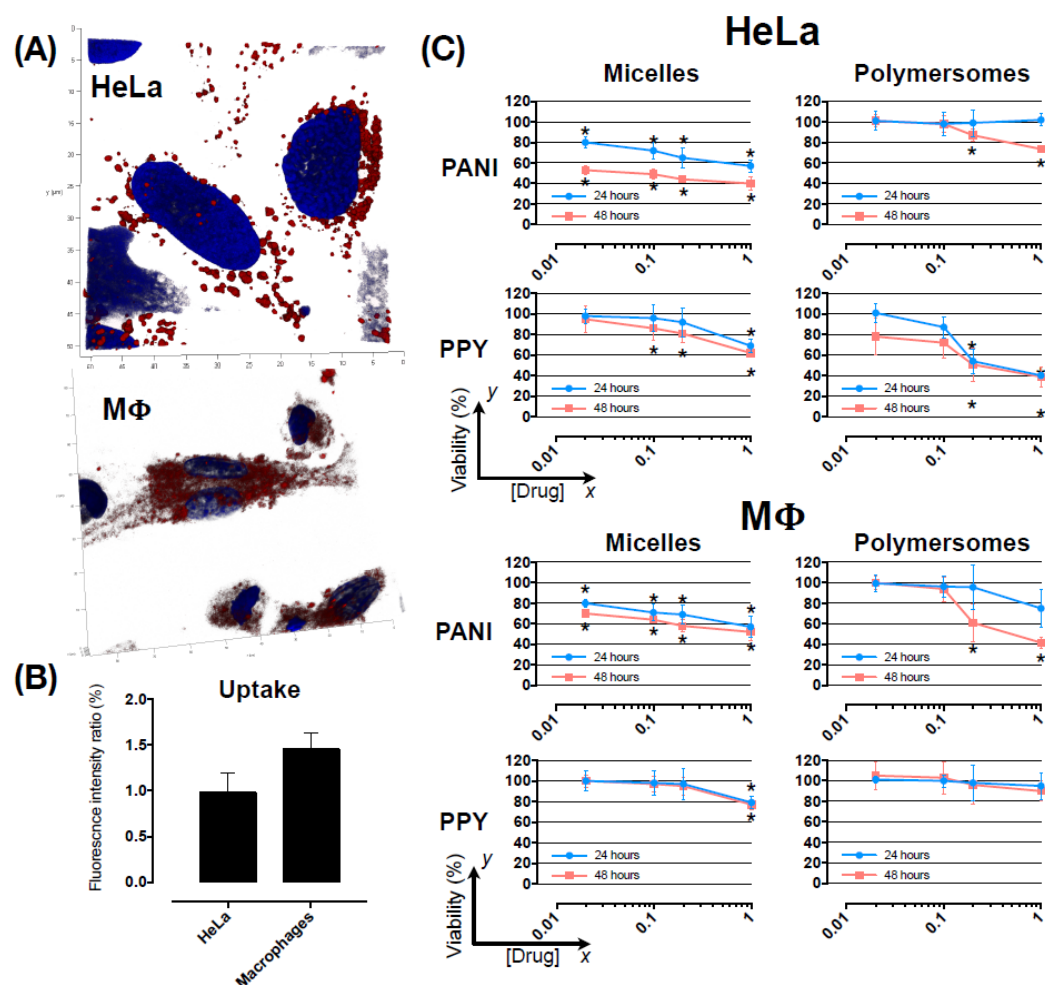


Figure 4. Interactions of CP-based nanoparticles with cells. (A) 3D-confocal microscopy for uptake imaging using Which one?-functionalised PPy nanospheres. (B) Quantification of uptake. (C) Cell metabolic assay (MTT) for PANI and PPy nanospheres and nanovesicles. Concentration tested: 1, 0.2, 0.1, 0.02 mg mL⁻¹. $n = 3$ independent experiments. Statistic: t -test with $*p < 0.05$ compared to untreated cells.

Finally, CP-based colloids were examined as a bio-imaging platform and their potential of modulating cell metabolic activity was explored. Confocal-based uptake experiments revealed that the dye-functionalised PPy nanospheres were efficiently taken-up by both HeLa and MΦ cells, with a tendency of MΦ in engulfing more particles (Figure 4 A&B). Interestingly, while the PPy particles remained intact in HeLa, they appeared to degrade in MΦ (Figure 4A), which is likely due to the harsher cytosolic environment typical of professional phagocytes. Figure 4C (top left) illustrates that the PANI nanospheres possess a concentration-dependent toxicity in HeLa after 24 hours, with more pronounced effects after 48 hours. In comparison, the PPy nanospheres appeared to be more biocompatible, especially after 48 hours of incubation. Figure 4C (top right) shows that PANI nanovesicles were completely biocompatible in HeLa after 24 hours, with a moderate decrease in cell viability detected after 48 hours, only for the highest concentrations tested. Similar effects have been observed for the PPy nanovesicles. The results described for the HeLa cells follow

a similar trend in $M\Phi$. The only difference concerns the PPy nanovesicles, which were highly biocompatible in all the conditions tested.

In conclusion, we demonstrated, for the first time, a facile and effective one-pot route that combines PISA process and conventional oxidative polymerisation to prepare a range of hybrid polymer-organic nanoparticles. This highly versatile synthetic approach utilizes the selective localization of oxidising agent in the PISA-prepared nanoparticle templates to direct the formation of conjugated polymer and give access to morphologies not typically achievable *via* other routes. Ferric (III) salt is complexed into the PHPMA block enabling the preparation of the PPy- and PANI-based nanospheres and nanovesicles, while the PMPC block confers biocompatibility and steric stabilization. Upon transient NIR laser irradiation, all the CP-based particles exhibit good photostability and rather high photothermal conversion efficiency due to their strong NIR absorption, as deduced by UV-vis spectrometer. These CP-based hybrid nanoparticles could be utilized as promising NIR photothermal transducers for localized tumorous hyperthermia therapy. Moreover, it becomes clear that the wide variety of PISA formulations available and the ease to tailor functionality and chemistry of PISA-prepared nanoparticles will open entirely new opportunities for the fabrication of hybrid materials, in particular polymer-organic nanocomposites. Therefore we believe that our process route will be of great interest for various applications in the biomedical fields, such as bio-imaging, nanomedicine and optogenetics.

Methods

Materials. All chemicals were purchased from the Sigma-Aldrich Chemical Company and used as received unless otherwise noted. 2-Hydroxypropyl methacrylate (HPMA) was purchased from Aldrich and contains an isomeric mixture of 75 mol% HPMA and 25 mol% 2-hydroxyisopropyl methacrylate. Cyanine5 amine (Cy5 amine) was purchased from Lumiprobe Chemical Company. Semi-permeable cellulose tubing was purchased from SPECTRA/POR (molecular weight cut-off is 1000 Da).

RAFT Polymerisation-induced Self-Assembly. Poly[2-(Methacryloyloxy)ethyl phosphorylcholine] (PMPC) homopolymer and PMPC-*block*-PHPMA diblock copolymers were synthesized by RAFT according to a literature protocol.³³ Briefly, 4,4'-azobis(4-cyanovaleric acid) (V-501) (22.8 mg, 0.08 mmol) and 4-cyanopentanoic acid dithiobenzoate (CPADB) (113 mg, 0.406 mmol) were firstly dissolved in 5 wt% sodium bicarbonate aqueous solution. A solution of MPC (3 g, 10.2 mmol) in Milli-Q water (15.6 g) was then added to the reaction mixture. The solution was purged with nitrogen for 40 min and then placed in a pre-heated oil bath at 70 °C for 2 h under continuous stirring. At the end of the polymerization, the reaction was ceased via rapid cooling in an ice/water bath and exposure to air. The crude product was subject to ¹H NMR analysis to calculate monomer conversion and was then purified by dialysis against Milli-Q water. The final pure product was obtained by lyophilization.

In a general RAFT PISA formulations of diblock copolymer synthesis at 10 wt% total solids, a solution of PMPC₄₃ (0.1 g, 0.008 mmol), V-501 (0.7 mg, 0.003 mol) and HPMA (0.65 g, 4.5 mmol) in Milli-Q water (6.8 g) was degassed under nitrogen for 40 min before placing in a pre-heated oil bath at 70 °C for 24 h under continuous stirring. At the end of the reaction, the polymerization was quenched via rapid cooling in an ice/water bath and exposure to air. The crude product (0.1 mL) was collected and subject to ¹H NMR analysis to calculate monomer conversion.

Synthesis of Conjugated Polymer Nanoparticles. A general procedure for the synthesis of polypyrrole nanospheres via chemical oxidation is as follows. A solution containing iron(III) chloride (18.7 mg, 0.12 mmol) and a diluted aqueous dispersion of PMPC₄₃-*b*-PHMPA₂₅₈ (1 mL, 0.7 wt% total solids) was added to a reaction vessel equipped with a magnetic stir bar. The reaction vessel was sealed and the solution was stirred or sonicated either at room temperature or at 0 °C for 1 h. Subsequently, pyrrole (3.4 mg, 0.05 mmol) was slowly added to the reaction mixture and the solution was continuously stirred or sonicated either at room temperature or at 0 °C for 4 h. At the end of the reaction, the resulting nanoparticles were purified by dialysis against Milli-Q water. Syntheses of polypyrrole nanovesicles, polyaniline nanospheres and nanovesicles were performed in a similar fashion.

To investigate the effect of iron/PHPMA complexation on the formation of PPy nanospheres, the [FeCl₃]/[OH] (the hydroxyl group in PHPMA) molar ratio was varied from 0.5 to 10.4 with a fixed [FeCl₃]/[pyrrole] molar ratio of 2.3. A clear dependence of particle size and morphologies was observed by transmission electron microscopy (TEM) and dynamic light scattering (DLS) analysis (see the supporting information). For systems using PMPC-*b*-PHPMA spherical templates, an optimized [FeCl₃]/[OH] molar ratio of 3.2 was found to produce uniform PPy nanospheres. At higher molar ratio, the formation of PPy also appeared on the particle surfaces. Further increase of this ratio leads to the formation of a macroscopic black precipitate consistent with the limited solubility features of PPy in water and the absence of the PMPC chains as a

stabilising block. At low molar ratio, however, yellow milky dispersions were observed. This clearly suggests that there is little, or no, formation of PPy, but more likely oligopyrrole, under these conditions. Intriguingly, large variations in colloidal stability could be found when the post-PISA reaction temperature and the mixing method were varied. Lowering the temperature to ~ 0 °C or mixing the reaction ultrasonically during post-PISA treatment results in large agglomerations – indication of the promise of this fabrication approach to produce CP at different length scale.

Functionalisation of Conjugated Polymer Particles with Fluorescent Dye Cy5.

Polypyrrole Nanospheres (7 mg) was dispersed in 1 mL PBS buffer solution (pH 5, adjusted using 1 M HCl) in a 10 mL round bottom flask, followed by the addition of 1-ethyl-3-(3-dimethylaminopropyl) carbodiimide (EDC, 2.0 mg, 1.04×10^{-5} mol) and N-hydroxysuccinimide (NHS, 4.0 mg, 3.47×10^{-5} mol). The reaction mixture was stirred for 5 min at ambient temperature. Cyanine5 amine (Cy5 amine, 1.0 mg, 1.53×10^{-6} mol) was then added to the reaction flask and the reaction mixture was stirred overnight at ambient temperature. At the end of the reaction, the functionalized particles were purified through dialysis against water for 2 days.

Dynamic light scattering. The average particle size in the PPy and PANI dispersions was determined by dynamic light scattering using a Malvern Instrument Zetasizer Nano Series instrument. The scattered light was detected at an angle of 173° . For sample preparation, all dispersions were diluted to minimize the interaction between the nanoparticles.

UV-vis absorption. The absorption spectra of the PPy and PANI dispersions were recorded using a Perkin Elmer Lambda 25 UV-vis spectrometer. For sample preparation, all the polymer dispersions were diluted with Milli-Q water. pH-responsive PANi nanospheres were diluted either with water (pH neutral) or with acidic water (pH 4) before the measurement.

Fourier transform infrared (FTIR) spectroscopy. FTIR spectroscopy was conducted on a Bruker IFS 66/S instrument under attenuated total reflectance (ATR). An average of 64 scans were performed on each sample. The results were analyzed using OPUS software version 4.0.

Nuclear Magnetic Resonance (NMR) spectroscopy. NMR spectroscopic measurements were conducted on a Bruker DPX 300 instrument at 300 MHz for hydrogen nuclei. The internal solvent signal of D_2O ($\delta(D_2O) = 4.79$ ppm) was used as reference. ^{13}C solid-state NMR was performed on the freeze-dried samples of PPy and PANI nanospheres. Magic-angle spinning (MAS) spectra were acquired on a Bruker ASCEND (300 MHz) spectrometer. The measurement was performed utilizing 8 kHz MAS, a 1 s recycle delay, 23k scans and a 1 ms ramped cross polarization time at 25 °C.

Photothermal performance. Thermal images were captured by an SC300 infrared camera (Fluke TiR, USA) and analyzed by Examin IR image software (FLIR). The excitation source was an 808 nm diode-pumped continuous-wave solid-state laser system (LASERGLow Technologies, Shanghai, China).

To measure the photothermal performances of the samples, an 808 nm NIR laser was employed to deliver perpendicular through a quartz cuvette containing aqueous

dispersion (0.5 mL) of the sample with concentration of 0.2 mg mL⁻¹ or 1.0 mg mL⁻¹. Water was used as a control. The NIR laser light source was equipped with a power of 1.5 W cm⁻² under the 808 nm semiconductor laser device with a 5 mm diameter laser module. The temperature was measured using a thermocouple thermometer that was inserted into the aqueous dispersion perpendicular to the path of the laser light.

The photothermal conversion efficiency of the sample was determined according to the reported method.^{34,30} To measure the photothermal conversion efficiency (η), the aqueous dispersion samples were exposed to 808 nm NIR laser (1.5 W cm⁻²) for 600 s, and then the laser was shut off. The heating and cooling temperature trends of samples were recorded by temperature gauge. The photothermal conversion efficiency was calculated according to the eq 1:

$$\eta = \frac{hS(T_{max}-T_{surr})-Q_0}{I(1-10^{-A808})} \quad (1)$$

Where h is the heat transfer coefficient, S is the sample container surface area, T_{max} is the steady state maximum temperature, T_{surr} is the ambient room temperature, Q_0 is the baseline energy input by the solvent and the sample container without NPs, I is the laser power, and $A808$ is the absorbance of NPs at 808 nm.

In order to get the hS , θ herein is introduced, which is defined as the ratio of $(T-T_{surr})$ to $(T_{Max}-T_{surr})$:

$$\theta = \frac{T-T_{surr}}{T_{Max}-T_{surr}} \quad (2)$$

Thus, the value of hS is calculated by eq 3:

$$\tau_s = \frac{C_d m_d}{hS} \quad (3)$$

Where τ_s is the characteristic thermal time constant, the mass of the nanoparticle solution (m_d) is g, and its heat capacity (C_d) is approximately 4.2 J g⁻¹ k⁻¹ (the heat capacity of water). The heat energy (Q_0) of the sample container and solvent without nanoparticles is referred to a literature value ($Q_0 = 3.5$ J) described elsewhere.^{34,30}

Transmission Electron Microscopy (TEM) imaging. Conventional and Energy filtered-TEM (EFTEM) imaging were performed using a JEOL JEM-2200FS TEM equipped with a field emission gun (FEG) at 200 kV, and an in-column Omega filter. Images were taken at a collection angle of 24.282 mrad and in parallel imaging conditions for TEM mode. The STEM mode image was taken under convergent beam conditions. Image J was used to measure the TEM-measured number averaged diameter of both the templates and the CP-based nanoparticles. Twenty nanoparticles were measured for each formulation taken from different areas of the grid and different batches to allow for good statistics.

The block copolymer templates, PMPC₄₃-*b*-HPMA₂₅₈ and PMPC₁₅-*b*-HPMA₄₄₅, were stained using a phosphotungstic acid (PTA) solution at 0.75 wt%. The solution was prepared by dissolving 37.5 mg of PTA in boiling distilled water (5 mL). The pH was adjusted to 7.0 by adding a few drops of 5 M NaOH under continuous stirring. The

PTA solution was then filtered through a 0.2 μm filter. Copper grids were glow-discharged for 40 seconds in order to render them hydrophilic. Then 5 μL of sample (concentration = 0.5 mg mL^{-1}) was deposited onto the grids for one minute. After that, the grids were blotted with filter paper and immersed into the PTA staining solution for 3 seconds for negative staining. Then the grids were blotted again and dried under vacuum for 1 minute. Fe^{3+} complexed PMPC₁₅-b-HPMA₄₄₅ nanovesicles and all the CP-based nanoparticles were imaged in absence of PTA staining.

Elemental analysis of the specimens was performed using the microscope in energy-filtered transmission electron microscopy (EF-TEM) mode with the aim to obtain fine structure imaging. The software used for image acquisition and processing was the Digital Micrograph™ software (version 3.20). Images were recorded using a charge coupled device (CCD) camera US1000XP from Gatan.

In EF-TEM mode, chemical mapping was achieved by selecting electrons that have lost a specific amount of energy from inelastic scattering. In the case of inner shell ionization, the energy loss is characteristic of the element the electron interacted with in the specimen. In the present study the elements investigated were Iron and Phosphorus. Conventional unfiltered TEM images and Iron/phosphorus maps were acquired. For the elemental maps electrons were collected post specimen and dispersed using the Omega filter. An electron energy loss spectrum (EELS) was traced across the dispersion plane. From the spectrum the region of interest was selected with an energy window; the subsequent insertion of an energy slit allowed for the image to be formed.

The Iron present in the structures was identified by exciting the atomic M shell with a slit width of 3 eV. The Iron ionisation energy in the $M_{2,3}$ edges is 54 eV. The Phosphorus element present in the imaged structures was identifying by exciting the atomic L shell with a slit of 10 eV. The Phosphorus ionisation energy in the $L_{2,3}$ edges is 132 eV. The 3-window technique was employed. This technique involves acquiring two images before and one after the ionization edge. The pre-edge images are used to compute the approximate background contained in the post-edge window. Once the background is determined and removed, the subsequent map displays a signal that is proportional to the element concentration in the sample. The first pre-edge, second pre-edge, and post-edge energies were 47.5 eV, 50.5 eV, and 55.5 eV respectively for Iron mapping. The first pre-edge, second pre-edge, and post-edge energies were 115 eV, 125 eV, and 137 eV respectively for Phosphorus mapping. The elastic TEM image and the false colour chemical mapping were superimposed using ImageJ software.

Relative thickness maps were also obtained in the EF-TEM technique by acquiring an unfiltered and zero-loss image from the same region under identical conditions. Thickness maps evaluate the sample local thickness in terms of electron mean free path (mfp). Electron mean free paths values between 1 and 2 represent the best sample thickness conditions for performing efficient elemental mapping.

Cell cultures, metabolic assays and confocal imaging. HeLa cells were cultured and maintained using DMEM containing: 10 (v/v) fetal calf serum, 2 mM L-glutamine, 100 mg/ml streptomycin and 100 IU/ml penicillin. Cells were cultured at 37 °C/95% air/5% CO₂. Cells were periodically sub-cultured using Trypsin-EDTA solution 0.25% for the detachment process and centrifuged at 2000 rpm for 5 minutes for the pellet collection. THP-1 were cultured and maintained in RPMI-1640 medium, supplemented with 10

mM HEPES buffer, and 10 (v/v) fetal calf serum, 2 mM L-glutamine, 100 mg/ml streptomycin and 100 IU/ml penicillin. THP-1 monocytes were differentiated to macrophages through incubation with 5 ng/mL of PMA for 48 hours.³⁵ We chose this PMA concentration as it has been found to not undesirably regulate genes expression.³⁶

For metabolic assay, the MTT method was used. Briefly, cells were seeded at a concentration of 5×10^3 cells/well in a 96 well plate overnight. Increasing concentrations of nanoparticles were then added in the growth media, namely 1, 0.2, 0.1, 0.02 mg mL⁻¹, for 24 and 48 hours. The medium growth was then removed, and the Tetrazolium Blue salt added for 2 hours. An acidified solution of isopropanol was then added to dissolve the water-insoluble MTT formazan. The solubilized blue crystals were measured colorimetrically at 570 nm (plate reader ELx800, BioTek).

For uptake imaging analyses, HeLa and THP-1 cells were seeded on glass-bottom petri dishes (Ibidi) at a concentration of 5×10^3 cells/well, and incubated with RhB-labeled nanoparticles (0.1 mg mL⁻¹) for 24 and 48 hours, followed by 3 steps of PBS washing. Cells were then stained with DAPI for nuclear staining, and imaged with confocal microscope (Leica SP8). For the uptake quantification, 10 different regions of the petri dishes were captured, and the fluorescent signal has been normalized to the nuclear intensity signal (using ImageJ).

References:

1. Xu, L.; Cheng, L.; Wang, C.; Peng, R.; Liu, Z., Conjugated polymers for photothermal therapy of cancer. *Polymer Chemistry* **2014**, *5*, 1573-1580.
2. Chiang, C. K.; Fincher Jr, C. R.; Park, Y. W.; Heeger, A. J.; Shirakawa, H.; Louis, E. J.; Gau, S. C.; MacDiarmid, A. G., Electrical conductivity in doped polyacetylene. *Physical review letters* **1977**, *39*, 1098.
3. Bhosale, M. E.; Illathvalappil, R.; Kurungot, S.; Krishnamoorthy, K., Conjugated porous polymers as precursors for electrocatalysts and storage electrode materials. *Chemical Communications* **2016**, *52*, 316-318.
4. Page, Z. A.; Chiu, C.-Y.; Narupai, B.; Laitar, D. S.; Mukhopadhyay, S.; Sokolov, A.; Hudson, Z. M.; Bou Zerdan, R.; McGrath, A. J.; Kramer, J. W.; Barton, B. E.; Hawker, C. J., Highly Photoluminescent Nonconjugated Polymers for Single-Layer Light Emitting Diodes. *ACS Photonics* **2017**, *4*, 631-641.
5. Wang, Y.; Li, S.; Zhang, P.; Bai, H.; Feng, L.; Lv, F.; Liu, L.; Wang, S., Photothermal - Responsive Conjugated Polymer Nanoparticles for Remote Control of Gene Expression in Living Cells. *Advanced Materials* **2018**, DOI: 10.1002/adma.201705418.
6. Lyu, Y.; Xie, C.; Chechetka, S. A.; Miyako, E.; Pu, K., Semiconducting Polymer Nanobioconjugates for Targeted Photothermal Activation of Neurons. *Journal of the American Chemical Society* **2016**, *138*, 9049-9052.
7. Molina, M.; Wedepohl, S.; Calderon, M., Polymeric near-infrared absorbing dendritic nanogels for efficient in vivo photothermal cancer therapy. *Nanoscale* **2016**, *8*, 5852-5856.
8. Feng, X.; Mao, C.; Yang, G.; Hou, W.; Zhu, J.-J., Polyaniline/Au Composite Hollow Spheres: Synthesis, Characterization, and Application to the Detection of Dopamine. *Langmuir* **2006**, *22*, 4384-4389.
9. Ahn, K.-J.; Lee, Y.; Choi, H.; Kim, M.-S.; Im, K.; Noh, S.; Yoon, H., Surfactant-Templated Synthesis of Polypyrrole Nanocages as Redox Mediators for Efficient Energy Storage. *Scientific Reports* **2015**, *5*, 14097.
10. Hong, J. Y.; Yoon, H.; Jang, J., Kinetic Study of the Formation of Polypyrrole Nanoparticles in Water - Soluble Polymer/Metal Cation Systems: A Light - Scattering Analysis. *Small* **2010**, *6*, 679-686.
11. Pecher, J.; Mecking, S., Nanoparticles of Conjugated Polymers. *Chemical Reviews* **2010**, *110*, 6260-6279.
12. Warren, N. J.; Armes, S. P., Polymerization-induced self-assembly of block copolymer nano-objects via RAFT aqueous dispersion polymerization. *Journal of the American Chemical Society* **2014**, *136*, 10174-10185.
13. Pei, Y.; Lowe, A. B.; Roth, P. J., Stimulus - Responsive Nanoparticles and Associated (Reversible) Polymorphism via Polymerization Induced Self - assembly (PISA). *Macromolecular rapid communications* **2017**, *38*, 1600528.
14. Teo, G. H.; Kuchel, R. P.; Zetterlund, P. B.; Thickett, S. C., Polymer-inorganic hybrid nanoparticles of various morphologies via polymerization-induced self assembly and sol-gel chemistry. *Polymer Chemistry* **2016**, *7*, 6575-6585.
15. Bleach, R.; Karagoz, B.; Prakash, S. M.; Davis, T. P.; Boyer, C., In Situ Formation of Polymer-Gold Composite Nanoparticles with Tunable Morphologies. *ACS Macro Letters* **2014**, *3* (7), 591-596.
16. Karagoz, B.; Yeow, J.; Esser, L.; Prakash, S. M.; Kuchel, R. P.; Davis, T. P.; Boyer, C., An Efficient and Highly Versatile Synthetic Route to Prepare Iron Oxide

Nanoparticles/Nanocomposites with Tunable Morphologies. *Langmuir* **2014**, *30* (34), 10493-10502.

17. Ma, C.; Liu, X.; Wu, G.; Zhou, P.; Zhou, Y.; Wang, L.; Huang, X., Efficient Way to Generate Protein-Based Nanoparticles by in-Situ Photoinitiated Polymerization-Induced Self-Assembly. *ACS Macro Letters* **2017**, *6*, 689-694.
18. Blanz, A.; Verber, R.; Mykhaylyk, O. O.; Ryan, A. J.; Heath, J. Z.; Douglas, C. W. I.; Armes, S. P., Sterilizable gels from thermoresponsive block copolymer worms. *Journal of the American Chemical Society* **2012**, *134*, 9741-9748.
19. Armes, S. P.; Vincent, B., Dispersions of electrically conducting polypyrrole particles in aqueous media. *Journal of the Chemical Society, Chemical Communications* **1987**, 288-290.
20. Yasuda, A.; Shimidzu, T., Chemical and electrochemical analyses of polyaniline prepared with FeCl₃. *Synthetic metals* **1993**, *61*, 239-245.
21. de Oliveira, H. P.; Andrade, C. A. S.; de Melo, C. P., Electrical impedance spectroscopy investigation of surfactant-magnetite-polypyrrole particles. *Journal of Colloid and Interface Science* **2008**, *319*, 441-449.
22. Panigrahi, R.; Srivastava, S. K., Ultrasound assisted synthesis of a polyaniline hollow microsphere/Ag core/shell structure for sensing and catalytic applications. *RSC Advances* **2013**, *3*, 7808-7815.
23. Forsyth, M.; Truong, V.-T.; Smith, M. E., Structural characterization of conducting polypyrrole using ¹³C cross-polarization/magic-angle spinning solid-state nuclear magnetic resonance spectroscopy. *Polymer* **1994**, *35*, 1593-1601.
24. Becker, A.; Hassenius, C.; Licha, K.; Ebert, B.; Sukowski, U.; Semmler, W.; Wiedenmann, B.; Grötzinger, C., Receptor-targeted optical imaging of tumors with near-infrared fluorescent ligands. *Nature biotechnology* **2001**, *19*, 327.
25. Bjorklund, R. B.; Liedberg, B., Electrically conducting composites of colloidal polypyrrole and methylcellulose. *Journal of the Chemical Society, Chemical Communications* **1986**, 1293-1295.
26. Yang, J.; Choi, J.; Bang, D.; Kim, E.; Lim, E. K.; Park, H.; Suh, J. S.; Lee, K.; Yoo, K. H.; Kim, E. K., Convertible Organic Nanoparticles for Near-Infrared Photothermal Ablation of Cancer Cells. *Angewandte Chemie International Edition* **2011**, *50*, 441-444.
27. Hahn, G. M.; Braun, J.; Har-Kedar, I., Thermochemotherapy: synergism between hyperthermia (42-43 degrees) and adriamycin (of bleomycin) in mammalian cell inactivation. *Proceedings of the National Academy of Sciences* **1975**, *72*, 937-940.
28. Guimard, N. K.; Gomez, N.; Schmidt, C. E., Conducting polymers in biomedical engineering. *Progress in Polymer Science* **2007**, *32*, 876-921.
29. Wang, N.; Yao, B. D.; Chan, Y. F.; Zhang, X. Y., Enhanced photothermal effect in Si nanowires. *Nano letters* **2003**, *3*, 475-477.
30. Ayala-Orozco, C.; Urban, C.; Knight, M. W.; Urban, A. S.; Neumann, O.; Bishnoi, S. W.; Mukherjee, S.; Goodman, A. M.; Charron, H.; Mitchell, T.; Shea, M.; Roy, R.; Nanda, S.; Schiff, R.; Halas, N. J.; Joshi, A., Au Nanomatryoshkas as Efficient Near-Infrared Photothermal Transducers for Cancer Treatment: Benchmarking against Nanoshells. *ACS Nano* **2014**, *8*, 6372-6381.
31. Chen, M.; Fang, X.; Tang, S.; Zheng, N., Polypyrrole nanoparticles for high-performance in vivo near-infrared photothermal cancer therapy. *Chemical Communications* **2012**, *48*, 8934-8936.

32. Zhou, J.; Lu, Z.; Zhu, X.; Wang, X.; Liao, Y.; Ma, Z.; Li, F., NIR photothermal therapy using polyaniline nanoparticles. *Biomaterials* **2013**, *34*, 9584-9592.
33. Sugihara, S.; Blanz, A.; Armes, S. P.; Ryan, A. J.; Lewis, A. L., Aqueous Dispersion Polymerization: A New Paradigm for in Situ Block Copolymer Self-Assembly in Concentrated Solution. *J. Am. Chem. Soc.* **2011**, *133*, 15707-15713.
34. Tian, Q.; Hu, J.; Zhu, Y.; Zou, R.; Chen, Z.; Yang, S.; Li, R.; Su, Q.; Han, Y.; Liu, X., Sub-10 nm Fe₃O₄@Cu₂-xS Core-Shell Nanoparticles for Dual-Modal Imaging and Photothermal Therapy. *Journal of the American Chemical Society* **2013**, *135*, 8571-8577.
35. Daigneault, M.; Preston, J. A.; Marriott, H. M.; Whyte, M. K. B.; Dockrell, D. H., The identification of markers of macrophage differentiation in PMA-stimulated THP-1 cells and monocyte-derived macrophages. *PloS one* **2010**, *5*, e8668.
36. Park, E. K.; Jung, H. S.; Yang, H. I.; Yoo, M. C.; Kim, C.; Kim, K. S., Optimized THP-1 differentiation is required for the detection of responses to weak stimuli. *Inflammation research* **2007**, *56*, 45-50.

Acknowledgements *Feel free to add anything relevant in this section*

This work is funded by the EPSRC (GB to fill...grant number). The analysis of the photothermal effects is supported by (LN to fill).

Author contributions

G.B. and Y.P. conceived and developed the project. L.R-P., L.R., N.L. and J.W. performed the material characterizations and analysed the data. All authors contributed to discussions and manuscript writing.